Ab initio calculations of strain fields and failure patterns in silicon nitride intergranular glassy films

Anil Misra, L. Ouyang, Jie Chen, W.Y. Ching

Ab initio calculations of strain fields and failure patterns in silicon nitride intergranular glassy films

A. MISRA*†, L. OUYANG‡, J. CHEN§ and W. Y. CHING§

†Department of Civil and Mechanical Engineering, University of Missouri-Kansas City, 5110 Rockhill Road, Kansas City, MO 64110, USA
‡Department of Mathematics and Physics, Tennessee State University Nashville, TN 37221, USA
§Department of Physics, University of Missouri-Kansas City, 5110 Rockhill Road, Kansas City, MO 64110, USA

(*Received 19 January 2007; accepted in revised form 26 April 2007*)

Theoretical experiments were performed on silicon nitride intergranular glassy film (IGF) models subjected to tensile loading using an accurate *ab initio* method. The results were used to investigate the strain fields within IGF models. The Green–Lagrange strain fields were calculated from the displacement gradients of the IGF models under various loads. Significant deviations from the first-order Cauchy–Born rule were observed for IGF models even under small load. The strain fields were also analysed to understand atomic-scale mechanisms that lead to intergranular and intragranular failures.

1. Introduction

Silicon nitride is a light, hard ceramic that has wide applications as a structural and electronic material. A unique feature in silicon nitride and other polycrystalline ceramics is the existence of thin glassy films between microcrystal grains with a narrowly distributed width of about 1 nm [1, 2]. Although the thin intergranular glassy films (IGF) occupy only a very small fraction of overall composition and volume, they have a profound effect on the physical and mechanical properties of silicon nitride. In fact, a small amount of rare earth doping in the form of sintering aid, which usually resides at or near the IGF, leads to significant enhancement in strength and toughness of polycrystalline ceramics [3, 4]. How the small doping affects the overall physical and mechanical properties is still a matter of intense current investigations [5–8]. Although several theories [9–13] have given qualitative explanations for the role of IGFs in silicon nitride, a quantitative connection between the structure of an IGF and the mechanical properties of silicon nitride in the presence of IGFs remains illusive, largely due to the complexity of the microstructures of the material. Traditional continuum mechanics becomes invalid as the structural heterogeneity shrink to nanometre scale where energy locality is no longer a good approximation.

*Corresponding author. Email: misraa@umkc.edu.

We have recently studied the electronic structure and bonding of supercell models of both clean and Y-doped IGFs in Si_3N_4 [14–16]. In this paper, we aim at understanding the effect of the nanometre size undoped IGF on its mechanical behaviour. We perform theoretical tensile experiments using accurate *ab initio* method and then analyse the deformation and the failure mechanism of a small section of silicon nitride containing IGF without any dopants based on data obtained from simulation. Our main result is the *ab initio* strain field distribution as a function of tensile loading. In the following section, we outline our computational method and modelling. The results on the strain fields and failure mechanism are then presented and discussed in section 3. The conclusions of this study are listed in the last section.

2. Computational method and model

The steps followed for *ab initio* strain field calculations in a silicon nitride IGF can be divided into three parts: (i) construction of a fully relaxed initial periodic super-cell atomic model of nanometre sized IGF sandwiched between β-Si_3N_4 crystals; (ii) stepwise deformation of the periodic super-cell under uniaxial strain loading; and (iii) analysis of the atomic positions at each load increment to develop local strain fields.

2.1. *IGF atomic model*

Figure 1 shows an atomistic view (798 atoms with periodic boundary conditions) of an intergranular thin film (IGF) of about 10 Å between basal [0001] surfaces of two Si_3N_4 crystallites. The dimensions of the fully relaxed unit cell containing the

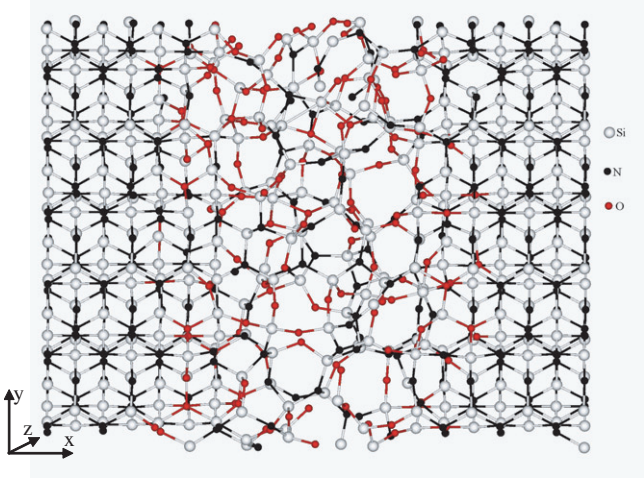

Figure 1. Ball–stick models of intergranular glassy film (IGF). The disordered IGF is about 1.3 nm thick.

IGF are $29.9 \times 22.7 \times 13.1$ Å. The initial model was constructed by classical molecular dynamics [14] and then fully relaxed using the VASP (Vienna *ab-initio* Simulation Package). VASP is a density functional theory based *ab initio* method using pseudopotentials and plane-wave expansion for the basis [17, 18]. The code has been one of the most popular electronic structure programs in recent years, especially for structural relaxation and geometry optimization. In the present study, a two-step relaxation process was adopted. First, the volume of the IGF was optimized followed by relaxation of all the atoms in the model. In the present calculation, we used GGA–Perdue–Wang–PAW potential with one general k-point and a relatively high energy cut-off of 400 eV. Because of the large unit cell, one general k-point is sufficient for the k-point sampling. The resulting energy and the residual force on each atom were converged to 0.001 eV and 0.01 eV Å^{-1}, respectively. In general, it takes 35 to 40 VASP relaxation steps to reach convergence. We have used the MPP machine Seaborg at the National Energy Supercomputing Center (NERSC) in Lawrence Berkeley Laboratory to carry out these simulations using 256, 512, and up to 1028 processors at different times. The IGF portion of the 798-atom model contains 76 Si, 112 O, and 50 N ions. The N/(O + N) ratio of 0.31 is close to the experimental value [4, 7]. The glassy structure in this IGF region is far from that of an ideal network in which Si is tetrahedrally bonded to either bridging O ions or threefold bonded N. There are a large number of under-coordinated Si and N.

2.2. *Atomistic simulation under mechanical loads*

The mechanical behaviour of the IGF model was investigated by two sets of theoretical uniaxial tensile experiments for different loading cases. In case 1, uniaxial strain was applied in incremental steps to the super-cell in small increments along the x-direction. The y- and z-dimensions of the model were kept constant while the x-dimension is increased such that the strain components were $\varepsilon_{xx} \neq 0$, while $\varepsilon_{yy} = \varepsilon_{zz} = 0$. Thus, for the x-direction loading, simulations were performed for the overall strain levels of $\varepsilon_{xx} = 0.23\%$, 0.46%, 0.93%, 1.38%, 1.85% and 2.31%. In case 2, uniaxial strain was applied to the super-cell along the y-direction. The x- and z-dimensions of the model were kept constant such that the strain components were $\varepsilon_{yy} \neq 0$, while $\varepsilon_{xx} = \varepsilon_{zz} = 0$. For the y-direction loading, simulations were performed for the overall strain-levels of $\varepsilon_{yy} = 2\%$, 4%, 6%, 8%, 10%, 12%, 14% and 16%. At each strain level, referred to the entire periodic model, all atoms in the model were fully relaxed using VASP until the residual force on each atom was reduced to less than 0.01 eV Å^{-1}. The relaxed model at a given strain serves as the starting position for the next increment of strain before the model is fully relaxed again. This process is carried on until the total energy (TE) and stress data show that the ''sample'' is fully fractured.

2.3. *Local strain field analysis*

At the end of each loading increment, the atoms displace to new equilibrium positions. Due to the presence of IGF, the atomic motions are expected to have a complex relationship to the applied strain. To analyse the patterns in the atomic

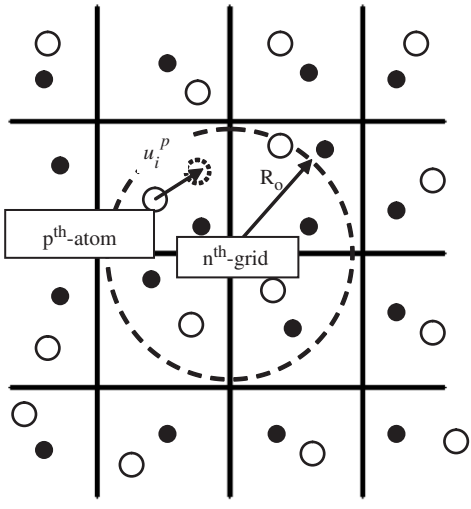

Figure 2. Schematic of grid used for local strain field analysis.

motions, we divide the super-cell into a $64 \times 50 \times 30$ grid and consider local groups of atoms contained within a sphere of radius R_o centred at the nth grid point as depicted in figure 2. We define a linear displacement field associated with the nth grid point, such that the displacement of pth atom within this group, is given as:

$$u_i^{np} = a_i^n + d_{ij}^n X_j^p \tag{1}$$

where u_i^{np} is the ith component of the fitted displacement for the pth atom, X_j^p is the position of the pth atom in the unstressed configuration, the coefficients a_i^n denote the rigid body displacement, and the coefficients d_{ij}^n represent the local displacement gradient. We can easily see that if all the atoms within a group move the same amount then equation (1) reduces to $u_i^{np} = a_i^n$. In this case, there is no relative movement between the atoms. Subscripts follow the usual tensor convention throughout this manuscript.

The coefficients a_i^n and d_{ij}^n in equation (1) are obtained by the minimization of the following function:

$$\sum_p \left(u_i^{np} - u_i^p\right)^2, \tag{2}$$

where u_i^p is the ith displacement component of pth atom obtained from the results of VASP simulation as follows:

$$u_i^{np} = x_j^p - X_j^p, \tag{3}$$

where x_j^p is the location of the pth atom in the deformed configuration. In our analysis, R_o is chosen to be 4.0 Å based upon two considerations: (i) to ensure a minimal local volume that guarantees the existence of solutions to the fitting process used to obtain the local displacement gradient; and (ii) to obtain a maximum resolution for the strain field in the IGF region. Too large a R_o will average out the

local variations and obscure the nonlinear behaviour of IGF under stress. On the other hand, a too small R_o will neglect the effects on the strain due to the atomistic motions of nearby atoms. Our experience shows that a choice of R_o of 4 Å is a reasonable one.

We note that the displacement field, $\bar{u}_i$, in continuum mechanics is usually expressed in terms of the mapping, Φ_i, that connects the deformed configuration to the unstressed reference configuration as follows [19]:

$$\bar{u}_i = \Phi_i(X_j) - X_i, \tag{4}$$

and the displacement gradient, d_{ij}, is written in terms of deformation gradient, F_{ij}, as

$$d_{ij} = \frac{\partial \bar{u}_i}{\partial X_j} = \frac{\partial \Phi_i(X_j)}{\partial X_j} - \delta_{ij} = F_{ij} - \delta_{ij}. \tag{5}$$

Thus, the local displacement gradient at the nth grid point, d^n_{ij}, defined in equation (1), may be used to obtain the local deformation gradient, F^n_{ij}, as follows:

$$F^n_{ij} = \delta_{ij} + d^n_{ij} \tag{6}$$

where δ_{ij} is the Kronecker delta. Consequently, the local Green–Lagrange strain tensor, ε^n_{ij}, is obtained as follows [19]:

$$\varepsilon^n_{ij} = \frac{1}{2}\left(F^n_{ik}F^n_{kj} - \delta_{ij}\right) \tag{7}$$

The local strain field describes the collective stiffness behaviour of a few atoms at various locations within the atomistic model. The local field will be analysed to understand how the material behaves under loading in terms of continuum mechanics.

3. Results and discussion

3.1. *Stress–strain behaviour of periodic cell*

When the periodic cell containing the IGF is subjected to tensile uniaxial strain loading, tensile stresses develop in both axial and lateral directions. Figures 3a and b show the axial stress component, σ_{xx}, and the lateral stress components, σ_{yy} and σ_{zz}, as a function of applied strains ε_{xx} and ε_{yy}, for x- and y-direction loadings, respectively. Figure 4 shows the evolution of total energy (TE) of the supercell with applied strain for both x- and y-direction loading. The stress–strain curves show an initial linear portion, then an onset of nonlinearity leading to a peak stress and an abrupt post peak softening. The TE shows an increase with applied strain until it reaches a plateau, indicating a complete separation or fracture of the periodic cell. We also note that at the atomistic scale of the periodic cell used in the simulation, the stress–strain behaviour and the TE variations are highly anisotropic.

For loading in the x-direction, the stress–strain response of the model is dominated by the behaviour of the IGF. We observe that the lateral stresses,

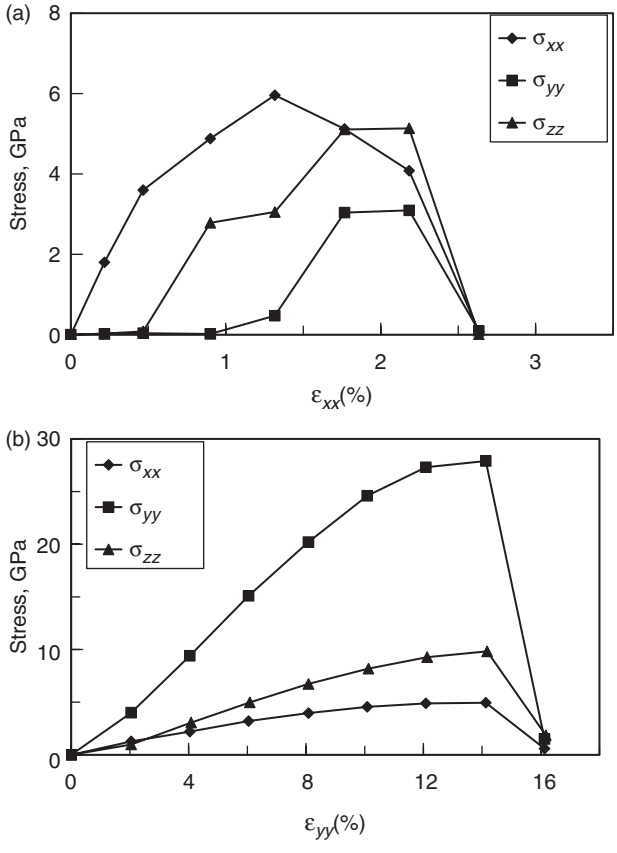

Figure 3. Stress–strain curve of the intergranular glassy film (IGF) model under (a) *x*-direction loading and (b) *y*-direction loading. Note the difference in the stress scale in (a) and (b).

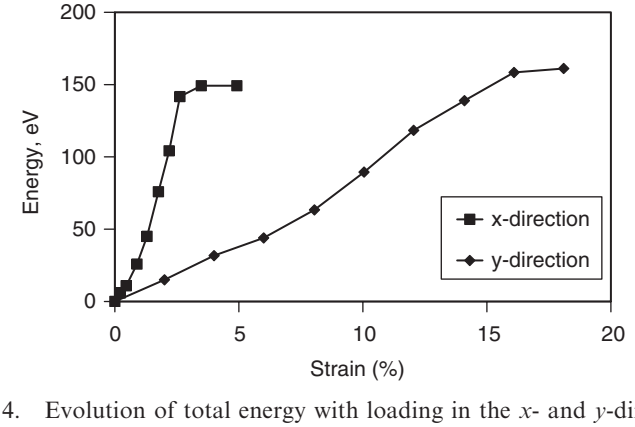

Figure 4. Evolution of total energy with loading in the *x*- and *y*-directions.

σ_{yy} and σ_{zz}, show very little increase in the first two load steps which correspond to the initial linear portion of the σ_{xx}–ε_{xx} curve. This stress–strain behaviour indicates that the initial atomic structure of the IGF is such that there is negligible coupling between the x- and the y–z directions. However, once the σ_{xx}–ε_{xx} behaviour becomes nonlinear for $\varepsilon_{xx} > 0.46\%$, the lateral stresses σ_{yy} and σ_{zz} increase rapidly. Clearly with increasing strain, the load carrying capacity of atomic interactions weakens in the x-direction, the structure adjusts such that load is carried through interactions in the y- and z-directions. It is noteworthy that this load induced evolution of the IGF atomic structure is such that the lateral stresses keep increasing even though the behaviour in the x-direction enters a softening regime at $\varepsilon_{xx} \geq 1.38\%$. Finally at $\varepsilon_{xx} \geq 2.31\%$, all the stress components enter a softening regime, indicating an overall failure of the material under the imposed loading path. Although the results from uniaxial strain loading cannot be directly compared to uniaxial stress experiments, the peak stress of 5.94 GPa at the strain of 1.38% can be interpreted as the IGF tensile strength. Experimental values of tensile strengths reported for silicon nitride have a wide variation attributable to a number of reasons, such as processing, testing methodology, presence of sintering agents, grain sizes, and porosities and other large-scale defects [20]. *Ab initio* calculations do not model these factors and do not include large-scale defects (see also Ogata *et al.* [21]). Furthermore, the tensile strength of the IGF may not be directly related to the tensile strength of a polycrystalline macroscopic sample in which IGF may be variously oriented with respect to the loading direction. Consequently, we expect that the calculated tensile strengths from *ab initio* calculations to be considerably larger than the experimental values. Therefore, it is remarkable that the calculated peak stress compares well with the tensile strength of 5.87 GPa reported by Edwards *et al.* [22] for Si_3N_4 based upon uniaxial stress lab experiments on thin films obtained from chemical vapour deposition process. The similarity in results could be due to relatively defect free microstructure with reduced glassy phase at grain boundaries possible in chemical vapour deposition process [23].

For loading in the y-direction, the stress–strain response of the model is completely different from the x-direction loading, and is dominated by the behaviour of the crystalline phase. We observe that up to the applied strain $\varepsilon_{yy} \approx 4.0\%$, the stress–strain behaviour is approximately linear. Assuming an isotropic behaviour within this strain level, we obtain a Young's modulus of 204 GPa and Poisson's ratio of 0.22, which compares well with the bulk elastic behaviour of Si_3N_4 polycrystallites (see Edwards *et al.* [22] and references therein). For applied strain $\varepsilon_{yy} \geq 4.0\%$, the stiffness of the periodic cell reduces and the behaviour becomes nonlinear. At a very large strain of $\varepsilon_{yy} \approx 14.0\%$, all the stress components enter a rapid softening regime leading to a complete rupture of the periodic cell.

3.2. *Local strain fields*

Local strain fields were computed from the atomic positions at each loading increment using equation (7). For further analysis, the strain components were averaged over the z-direction and plotted on the x–y plane. In figure 5, we have plotted the ε_{xx} component of the local strain field for x-direction loading. The local

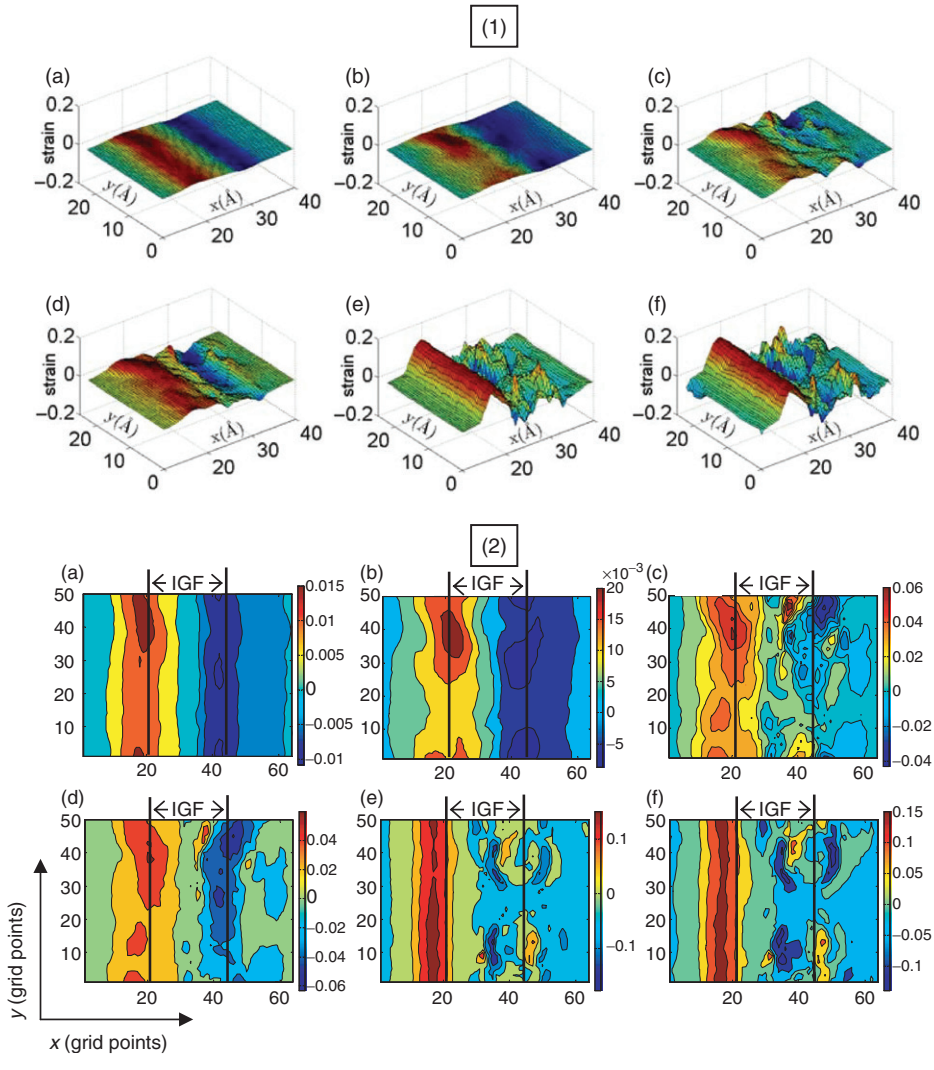

Figure 5. Local axial strains, ε_{xx}, plotted as (1) 3D surface plots and (2) 2D contour plots for x-direction loading at overall strain levels of (a) 0.23%, (b) 0.46%, (c) 0.93%, (d) 1.38%, (e) 1.85%, and (f) 2.31%, showing progressive development of tensile strain band along the interface between the intergranular glassy film (IGF) and crystalline layers, and compressive strain band within the IGF (See online for colour version).

strain field is shown both as surface and contour plots such that the local variations and their evolution with applied strain may be clearly visualized.

Furthermore, in figure 6, we show the ε_{yy} component of the local strain field for x-direction loading, and in figure 7 we show the ε_{xx} and ε_{yy} component of the local strain field for y-direction loading. Clearly, the local strain field is complex and highly heterogeneous. We also note that although the applied strain is uniaxial, multiaxial strains develop locally within the periodic cell. The calculated local strain fields show that local structures experience both normal as well as shear strains,

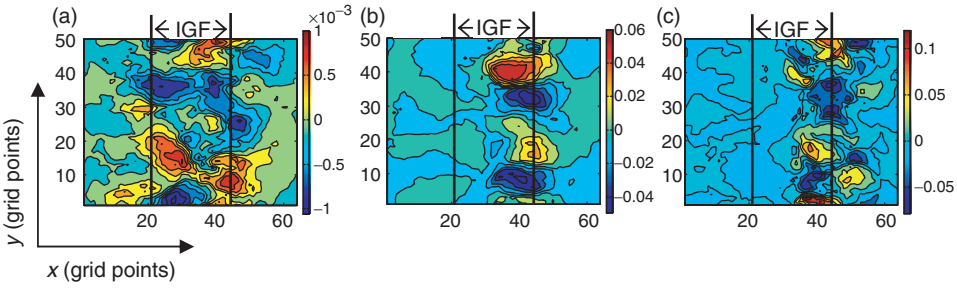

Figure 6. Contours of local lateral strains, ε_{yy}, for x-direction loading at overall strain levels of (a) 0.23%, (b) 0.93% and (c) 1.85% showing periodic compressive and tensile bands within the intergranular glassy film (IGF) (See online for colour version).

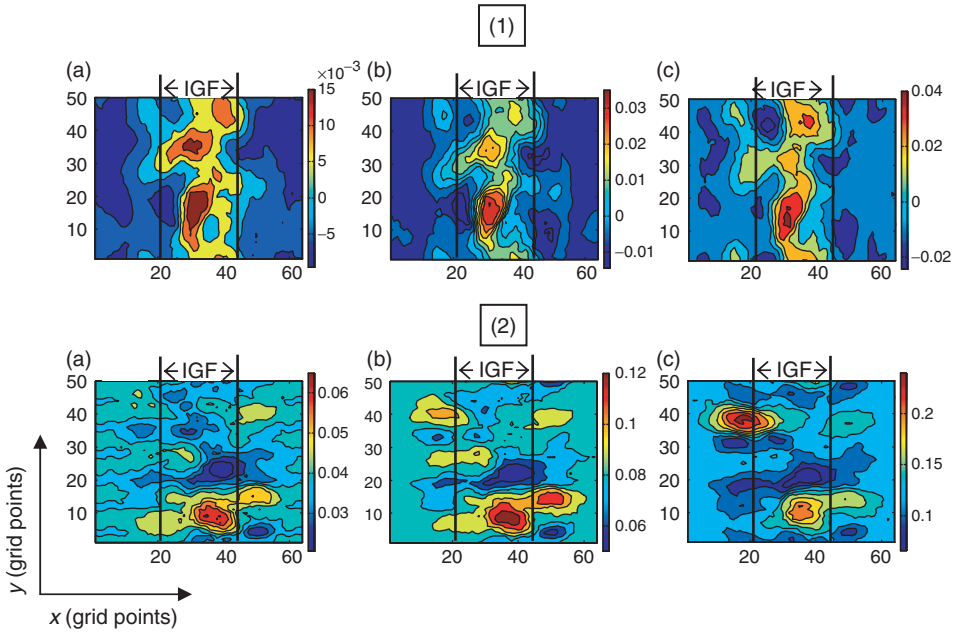

Figure 7. Contours of (1) local lateral strains, ε_{xx}, and (2) local axial strains, ε_{yy}, for y-direction loading at overall strain levels of (a) 4%, (b) 8% and (c) 12% (See online for colour version).

such that the strain tensor is fully populated. Such behaviour can only be revealed by detailed strain field analysis based on data obtained from rigorous *ab initio* quantum mechanical calculation.

From the strain field plots we observe that in the early part of the loading, when the stress–strain behaviour is linear, multiaxial strains occur at locations within the IGF and at the interface between the IGF and the crystalline phase. However, as seen from the lateral strain contours in figures 6 and 7, the locations of multiaxial strain spread into the crystalline phase as the loading progresses. Moreover, the magnitude and the variability of all the strain components evolve with loading.

To illustrate the evolution of multiaxial strains, we have calculated the frequency histograms of all the strain components. In figures 8 and 9 we have plotted the relative frequency distribution of the three normal strain components, ε_{xx}, ε_{yy} and ε_{zz}, for the x- and y-loading cases. We have also plotted the standard deviations of both normal and shear strain components. From the strain field plots as well as the frequency diagrams, we observe that there are many locations within the periodic cell where local strains are small or close to zero while the overall strain for the periodic cell is finite. Such cases especially arise close to failure where the local strain is concentrated in the failure zone. In these cases, the atoms in crystalline portion experience very little strain but large rigid body displacements, since they have moved substantially from their original positions. Clearly, the relationship between the local atomic motions and the overall strain of the periodic cell is extremely complex and significantly violates the Cauchy–Born rule [24]. Moreover, modifications or extensions to the Cauchy–Born rule, such as the use of higher order theories may also be insufficient. These results clearly indicate that for an accurate description of the continuum scale models of complex materials containing defects or microstructures, their behaviour at the atomistic level must be understood first.

The variations in local strain field reveal atomic-scale mechanisms that influence the overall stress–strain behaviour of the periodic cell containing the IGF. We observe from figures 5 and 6, that the applied strain in the x-direction is mostly accommodated by the IGF part of the model and the crystalline part experiences almost negligible strain during the linear part of the stress–strain curve ($\varepsilon_{xx} < 0.46\%$). Thus, the stress–strain response of the model under x-direction loading is dominated by the behaviour of the IGF. With loading, the crystalline part experiences increasingly higher strain, resulting in a strain gradient from the IGF region into the crystalline part as seen in figure 5. As a result, the bond lengths across the interface between the IGF and the crystalline layer increase. The large local tensile strains in figure 5 result from the relative movements between the atoms in the crystalline layers and the atoms within the IGF. As these interfacial bonds become progressively weaker, the bond lengths within the IGF shorten. Consequently, regions of compressive strains develop within the IGF and its close neighbourhood even though the overall strain is tensile for the periodic cell. As the loading progresses, these locations evolve into a persistent tensile strain concentration band along the interface between the IGF and crystalline layers, and compressive strain concentration band within the IGF.

The overall nonlinearity in the stress–strain behaviour is caused by the progressive weakening induced due to the strain concentrations within the bands. As can be seen in figure 6, the strain concentrations result in an interesting periodic pattern in the lateral strain field, ε_{yy}, composed of alternate bands of compressive and tensile strains. We also note that as the x-direction becomes weaker the loading is transferred to y-direction bonds or vice versa as revealed by increasing local lateral normal strains and shear strains. Although the average lateral normal strains and shear strains vanish, and therefore are consistent with the overall uniaxial loading, substantial local strains are observed as shown by the relative frequency distributions and the standard deviations of normal and shear strain components given in figure 8.

Under y-direction loading, the pattern of deformation is significantly different. As seen from figure 7, the strain field, ε_{yy}, in the direction of loading is characterized

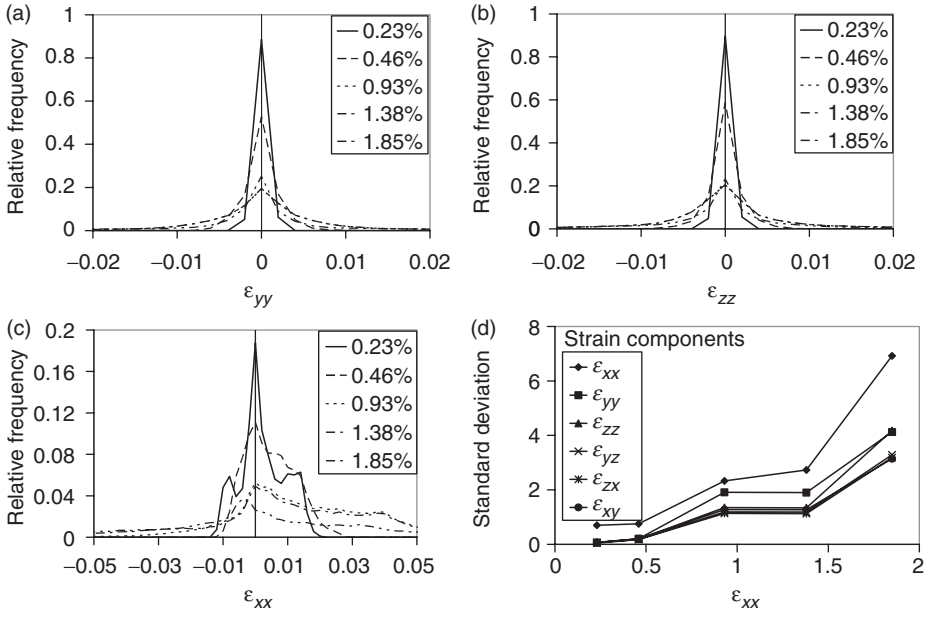

Figure 8. Frequency distributions of local strain field components (a) ε_{yy}, (b) ε_{zz} and (c) ε_{xx}, and (d) the standard deviations of all local strain field components for the x-direction loading.

by alternate bands of high and low strains whose average is consistent with the overall applied strain. These strain bands also initiate within the IGF and spread into the crystalline parts. This banded pattern is caused by neighbouring soft and stiff regions within the IGF. Under an applied tensile strain, the soft region is easily deformed and consequently undergoes further softening. Thus, the soft region attracts progressively higher strain while the neighbouring stiff region becomes stiffer as the applied loading increases. We also observe from figure 7, that the lateral strains, ε_{xx}, are compressive in the crystalline region and tensile in the IGF. Thus, the deformation pattern and the eventual failure under y-direction loading are also influenced by the structure of the IGF. Furthermore, as in the case of x-direction loading, y-direction loading also results in significant magnitudes of local shear strains as well as large heterogeneity in the strain fields, as shown in figure 9.

3.3. *Failure mechanisms*

Failure initiates at points that may be described as defect structures consisting of atoms that are either under-coordinated or over-coordinated. These points serve as local soft spots or stiff spots and, thus, attract higher deformations or forces. Typically, as the loading progresses, the soft locations deform under tension (strain concentration) and become weaker; at the same time the contiguous locations undergo local compressive strains and stiffen up. The result is that local soft spots get progressively weakened resulting in a global failure of the periodic cell. An analysis

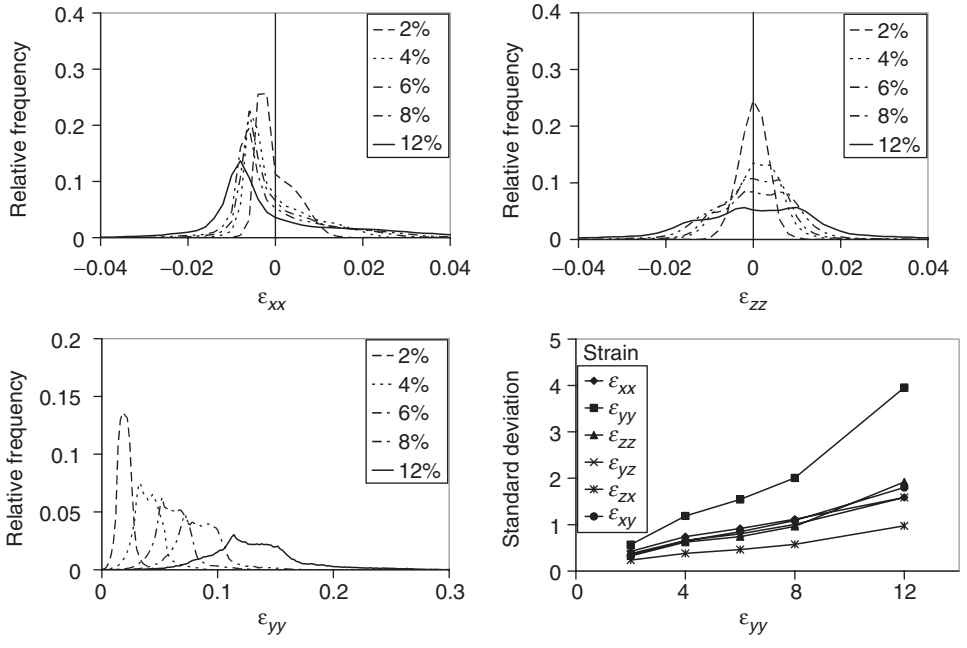

Figure 9. Frequency distributions of local strain field components (a) ε_{xx}, (b) ε_{zz} and (c) ε_{yy}, and (d) the standard deviations of all local strain field components for the *y*-direction loading.

of strain fields shown in figures 5–7 can provide insights to both intergranular and intragranular failure mechanisms.

The strain field given in figure 5 shows that the largest tensile strains obtained from *ab initio* calculation occur at the interface between the IGF glassy region and the Si_3N_4 crystalline grain. In addition, we observe that the large tensile strains are accompanied by compressive strains within the IGF as it shrinks towards the intact interface. Thus, the intergranular failure occurs as the soft spots at the interface weaken while stiff spots strengthen under loading. In recent years, an experimental procedure for direct observation of intergranular cracks in Si_3N_4 using transmission electron microscope (TEM) has been reported by Ii *et al.* [25]. In their procedure, microindentation is performed inside a TEM using a 1 μm indenter driven by a piezo-actuator with step size as low as 0.16 nm. Specimens of size $2 \times 2 \times 0.1$ mm are used and HREM images are acquired during stepwise indentation. We observe close qualitative agreement of failure mechanism observed in these experiments and those revealed by the local strain fields. The intergranular crack propagation pathway observed by Ii *et al.* [25] always occurred at the interface between the IGF glassy region and the Si_3N_4 crystalline grain. Similar interfacial crack propagation has been observed by Blonski and Garofalini [26] in their molecular dynamics simulations of thin calcium silicate intergranular films sandwiched between alumina crystals.

Intragranular failure mechanisms are more complex. However, as revealed by the local strain fields from *y*-direction loading shown in figure 7, the IGF has an important role in providing the seed location from where the failure initiates. Again, as the soft spots in the IGF are unable to sustain further loading and attracts large

strain concentration, the contiguous crystalline part is also subject to higher strains. Consequently, the crystalline part becomes heterogeneous leading to regions of strain concentrations and overall intergranular failure.

4. Conclusions

We have studied the mechanical behaviour of a nanometre size IGF sandwiched between silicon nitride crystals. Although the thin IGF occupies only a very small fraction of overall composition and volume, it has a profound effect on the mechanical behaviour of silicon nitride. The nanometre scale mechanical behaviour of such multiphase systems is extremely complex and not easily accessible through either experimental or theoretical methods. In this paper, we have taken a theoretical approach and performed *ab initio* simulation of IGF models subjected to tensile loading. This is the first time such *ab initio* results have been obtained for large multiphase systems. To understand the deformation patterns and failure mechanisms at atomic scales we have developed a methodology for strain field analysis based upon the *ab initio* calculations. Several interesting results have been obtained for the first time. Significant deviations from the first-order Cauchy–Born rule were observed for IGF models even under small load. Furthermore, atomic-scale mechanisms that lead to intergranular and intragranular failure were revealed from the analysis of the strain fields. In the future we plan to develop methodologies that can utilize these results for continuum-level modelling of polycrystallites.

Acknowledgments

This work is supported by the US DOE under Grant NO. DE-FG02-84DR45170. This research used resources of NERSC supported by Office of Science of DOE under contract No. DE-AC03-76SF00098. AM is partially supported by NSF grant CMS-0506297.

References

[1] F.F. Lange, B.I. Davis and M.G. Metcalf, J. Mater. Sci. **18** 1497 (1983).
[2] H.-J. Kleebe, J. Ceram. Soc. Jpn **105** 453 (1997).
[3] Hoffmann, M.J., in *Tailoring of Mechanical Properties of* Si_3N_4 *Ceramics*, edited by M.J. Hoffmann and G. Petzow, (Kluwer Academic, Dordrecht, 1994).
[4] E.Y. Sun, P.F. Becher, K.P. Plucknett, *et al*., J. Am. Ceram. Soc. **81** 2831 (1998).
[5] C.-M. Wang, X. Pan, M.J. Hoffmann, *et al*., J. Am. Ceram. Soc. **79** 788 (1996).
[6] H. Gu, X. Pan, R.M. Cannon, *et al*., J. Am. Ceram. Soc. **81** 3125 (1998).
[7] M.J. Hoffmann., H. Gu and R.M. Cannon, in *Interfacial Engineering for Optimized Properties II*, MRS Proceedings 586, edited by C.B. Carter, E.L. Hall, C.L. Briant, S. Nutt (Materials Research Society, Warrendale, PA, 2000).

[8] N. Shibata, S.J. Pennycook, T.R. Gosnell, *et al*., Nature **428** 730 (2004).
[9] D.R. Clarke, J. Am. Ceram. Soc. **70** 15 (1987).
[10] D.R. Clarke, T.M. Shaw, A.P. Philipse, *et al*., J. Am. Ceram. Soc. **76** 1201 (1993).
[11] M. Bobeth, D.R. Clark and W. Pompe, J. Am. Ceram. Soc. **82** 1537 (1999).
[12] R.H. French, J. Am. Ceram. Soc. **83** 2117 (2000).
[13] Cannon, R.M., Rühle, M., Hoffmann, M.J., *et al*., in *Grain Boundary Engineering in Ceramics*, Ceramic Transactions 118, edited by T. Sakuma, L.M. Sheppard, Y. Ikuhara (American Ceramic Society, Westerville, Ohio, 2000).
[14] P. Rulis, J. Chen, L. Ouyang, *et al*., Phys. Rev. B **71** 235317-1 (2005).
[15] J. Chen, P. Rulis, L. Ouyang, *et al*., Phys. Rev. Lett. **95** 256103 (2005).
[16] W.Y. Ching, J. Chen, P. Rulis, *et al*., J. Mater. Sci. **41** 5061 (2006).
[17] G. Kresse and J. Furthmuller, Comput. Mater. Sci. **6** 15 (1996).
[18] G. Kresse and J. Furthmuller, Phys. Rev. B **54** 11169 (1996).
[19] L.E. Maluern, *Introduction to the Mechanics of Continuous Medium* (Prentice-Hall, New Jersey, 1969).
[20] A. Diaz, S. Hampshire, J.F. Yang, *et al*., J. Am. Ceram. Soc. **88** 698 (2005).
[21] S. Ogata, N. Hirosaki, C. Kocer, *et al*., Phys. Rev. B **64** 172102-1 (2001).
[22] R.L. Edwards, G. Coles and W.N. Sharpe, Expl. Mech. **44** 49 (2004).
[23] O.R. Monteiro, Z. Wang and I.G. Brown, J. Mater. Sci. **31** 6029 (1996).
[24] M. Born and K. Huang, *Dynamical Theory of Crystal Lattices* (Clarendon, Oxford, 1956).
[25] S. Ii, C. Iwamoto, K. Matsunga, *et al*., Phil. Mag. **84** 2767 (2004).
[26] S. Blonski and S.H. Garofalini, J. Am. Ceram. Soc. **80** 1997 (1997).